Nanoscale



PAPER View Article Online



Cite this: DOI: 10.1039/d5nr03629a

Cellulose nanopaper with polymeric nanoparticle additives — what is the role of nanoparticle surface functionality?

Polymeric nanoparticles with tunable surface functionalities were synthesized *via* polymerization-induced self-assembly (PISA) to study their interactions with TEMPO-oxidized cellulose nanofibrils (TO-CNFs) in wet and dry states. The nanoparticles possessed a rigid core and shells featuring anionic, polyethylene glycol (PEG)-like, and hydroxyl-rich functionalities, with different hydrogen bonding propensities, water binding, and glass transition temperatures. Hydroxyl-functional nanoparticles exhibited enhanced and irreversible adsorption onto CNFs compared to anionic and PEG-like functions, showing that shell functionality impacts the adsorption behavior in the wet state. In the dry state, shell functionality plays a minor role in the bulk mechanical properties, which depend instead on the nanoparticle amount. This work shows that additive interactions between colloidal components in water do not translate to interactions in the dry state.

Received 27th August 2025, Accepted 16th October 2025 DOI: 10.1039/d5nr03629a

rsc.li/nanoscale

Introduction

Cellulose nanofibrils (CNFs) are promising bio-based building blocks for the development of advanced materials within the fields of packaging, electronic substrates, membranes, and separators. Produced from lignocellulosic biomass through chemical and mechanical treatments, CNFs form aqueous dispersions of long, slender fibrils with diameters of a few nanometers and lengths up to a micrometer, often stabilized by charged groups. Their high aspect ratio, surface area, and surface charge density enable surface engineering and tunable interactions. While CNF-based materials exhibit considerable potential for material assemblies, further systematic investigations of their structure–property relationships are essential to further advance their use in nanostructured, sustainable materials.

One promising strategy for tailoring the properties of CNF-rich materials is the incorporation of hydrophobic polymers from aqueous dispersions.^{4–9} This aqueous approach enables the introduction of hydrophobic polymers without the need for time-consuming solvent exchange and preserves the integrity of the cellulose surface by avoiding covalent modification.^{10,11} However, the dependencies on dispersion features such as particle size and surface functionality have yet to be fully elucidated.

Polymerization-induced self-assembly (PISA) offers an attractive platform for addressing these challenges. Exploiting controlled radical polymerization, PISA enables the one-step synthesis of colloidally stable block copolymer nanoparticles. This technique provides access to monodisperse nanoparticles with tunable size, shape, and surface characteristics, while eliminating the need for small-molecule stabilizers such as surfactants, which may interfere with cellulose interactions or migrate within dried materials. Such nanoparticles are therefore well suited for investigating how the surface and core functionality influence the performance of CNF-based composites.

The incorporation of nanoparticles into CNF dispersions typically involves combining preformed colloidal dispersions of each component. Depending on the extent of adsorption between nanoparticles and CNFs, different structures may arise in dispersion: CNFs may wrap around nanoparticles, cross-linking points may form, or phase-separated coacervates may develop. ^{14,15} In the absence of adsorption, homogeneous

^aKTH Royal Institute of Technology, Department of Fiber and Polymer Technology, School of Engineering Sciences in Chemistry, Biotechnology and Health, Teknikringen 56, SE-100 44 Stockholm, Sweden. E-mail: mavem@kth.se

^bFibRe – Centre for Lignocellulose-based Thermoplastics, KTH Royal Institute of Technology, Department of Fiber and Polymer Technology, School of Engineering Sciences in Chemistry, Biotechnology and Health, Teknikringen 56, SE-100 44 Stockholm. Sweden

^cWallenberg Wood Science Center, Department of Fibre and Polymer Technology, KTH Royal Institute of Technology, Teknikringen 56-58, SE-100 44 Stockholm,

^dDepartment of Bioproducts and Biosystems, Aalto University, Vuorimiehentie 1, 02150 Espoo, Finland

Paper Nanoscale

mixtures of the two components are expected. 16 Adsorption in these systems can typically be induced by increasing the ionic strength, which screens electrostatic repulsion. 11 Upon dewatering, the final structure of the material is determined by both the dispersion-state assemblies and their packing behavior during drying. Previous studies have shown that strongly adsorbing cationic nanoparticles of different sizes disrupt carboxyl-functional TEMPO-oxidized TO-CNF arrangements at multiple length scales, with the resulting CNF packing directly affecting bulk mechanical properties.³

In a dry material, the mechanical properties of CNF-based composites are governed by both the dispersion-induced structures and the inter-component interactions. Cationic polymeric nanoparticles have been reported to enhance ductility at high nanoparticle loadings, likely due to the ability of the two components to slide relative to one another and thereby dissipate stress.¹⁷ Consequently, the physicochemical characteristics of nanoparticle surfaces are expected to play a key role in determining the extent and nature of mechanical property modifications in CNF-rich materials.

In the present work, we synthesize colloidal nanoparticles with novel types of shell functionalities and investigate their influence on the mechanical properties of TO-CNF films. The nanoparticles are stabilized by shells of poly(methacrylic acid) (PMAA), poly(oligoethylene glycol methacrylate) (POEGMA), and poly(glycerol monomethacrylate) (PGMA), respectively. These nanoparticle surfaces have different potentials for hydrogen bonding, water binding, and glass transition temperatures.

Materials and methods

Materials

Methacrylic acid (MAA) (99%), oligo(ethylene glycol) methyl ether methacrylate (OEGMA) with an $M_{\rm p}$ of 500, glycidyl methacrylate (GlyMA) (97%), and methyl methacrylate (MMA) (99%) were purchased from Sigma-Aldrich, and passed over basic alumina to remove the radical inhibitor prior to polymerization. Basic alumina (aluminium oxide 90 active basic (0.063-0.200 mm) activity stage I) was purchased from Merck Millipore. 1,4-Dioxane anhydrous (99%), diisopropyl ether (for synthesis), and 4.4'-azobis(4-cyanovaleric acid) (ACVA) (98%) were purchased from Sigma-Aldrich and used as received.

Never-dried sulfite pulp was kindly donated by Domsjö.

Synthesis of water-soluble oligomeric polymers (macroCTA)

The RAFT agent CTPPA was synthesized according to a previously published protocol. 18 The water-soluble oligomer, which formed the shell, was synthesized by solution polymerization.

Poly(methacrylic acid) (macroCTA_A) was synthesized in distilled water. The monomer was not purified to avoid deprotonation. To a round bottom flask were added CTPPA (832 mg; 1 eq.), ACVA (84 mg; 0.1 eq.), and MAA (6.33 ml; 6.46 mg; 25 eq.) to yield a yellow solution. 23.7 ml of distilled water was added, making a partly cloudy mixture with [MAA] = 2.5 M. The solution was cooled in an ice bath and bubbled with argon for 15 min, and then reacted in a pre-heated oil bath at 70 °C for 4 h. The conversion was calculated from ¹H NMR according to eqn (1), as 95%. The polymer was purified by dialysis, with a 1 kDa cutoff, and freeze-dried.

Poly(oligo(ethylene glycol) methyl ether methacrylate) (macroCTA_O) was synthesized in 1,4-dioxane. The monomer was purified by passing over basic alumina. To a roundbottom flask, CTPPA (111 mg; 1 eq.), ACVA (11 mg; 0.1 eq.), OEGMA (4.74 ml; 5 g; 25 eq.), and 1,4-dioxane (15.2 ml) were added to make [OEGMA] = 0.5 M. The solution was cooled in an ice bath and bubbled with argon for 15 min, and then reacted in a pre-heated oil bath at 70 °C for 24 h. The conversion was calculated from ¹H NMR according to eqn (1) as 97%. The polymer was precipitated from diisopropyl ether, redissolved in distilled water, and freeze-dried.

Poly(glycerol methacrylate) (macroCTA_G) was synthesized from glycidyl methacrylate (GlyMA). A 20 vol% solution of GlyMA in distilled water was heated to 80 °C for 20 hours using a condenser. The conversion calculated from ¹H NMR was 84%. To a round-bottom flask were added CTPPA (334 mg; 1 eq.), ACVA (33.75 mg; 0.1 eq.), monomer solution (20 ml; 5.3 g; 25 eq.), and distilled water to make [GMA] = 1.3 M. The solution was cooled in an ice bath and bubbled with argon for 15 min, and then reacted in a pre-heated oil bath at 70 °C for 4 h. The conversion was calculated from ¹H NMR according to eqn (1) as 98%. The polymer was purified by dialysis, with a 1 kDa cutoff, and freeze-dried.

The conversion of methacrylate monomer was analyzed by ¹H NMR by taking a crude aliquot of the reaction mixture and diluting in D2O. The intensity of the monomer peak at ~6.1 ppm (1H) was compared to those of polymer methyl signals at 1.2-0.7 ppm (3H).

Conversion (%) =
$$\frac{\frac{I_{1.2-0.7 \text{ ppm}}}{3}}{\frac{I_{1.2-0.7 \text{ ppm}}}{3} + \frac{I_{6.1 \text{ ppm}}}{1}} \times 100$$
 (1)

Polymerization-induced self-assembly (PISA)

The macroCTAs were chain extended with MMA in emulsion polymerization according to PISA principles. The dry content (macroCTA, initiator ACVA and MMA) was set at 10 wt% and the ratio I/CTA = 0.12. In a typical experiment, the macroCTA was added to a round-bottom flask and dissolved in water. ACVA was dissolved in water with 3.5 eq. of NaHCO₃ to make [ACVA] = 10 mg ml⁻¹. An appropriate amount of ACVA solution was added to the macroCTA solution. At this point, the solution of anionic macroCTA_A was modified to pH 5.5 with 1 M NaOH. The pH of the other macroCTAs was unmodified. The MMA was passed over basic alumina to remove the inhibitor, and then an appropriate amount of MMA was added to the solution. This results in an emulsion as the majority of MMA does not dissolve in the water phase. The solution was cooled in an ice bath and bubbled with argon for 15 min, and then reacted in a pre-heated oil bath at 70 °C.

Nanoscale Paper

The conversion of monomer in these chain-extension polymerizations was analyzed gravimetrically. Aliquots of 100 μl were taken from the reaction mixture and dried at 125 $^{\circ}C$ for 1 hour. The measurements were performed in triplicate.

Preparation of cellulose nanofibrils (CNFs)

TEMPO-oxidized CNFs (TO-CNFs) were prepared according to previously described procedures. 19,20 Never-dried softwood sulfite pulp (Domsjö) was treated with TEMPO-mediated oxidation at pH 6.8 in phosphate buffer (0.05 M) and fibrillated in a high-pressure homogenizer (Microfluidizer M-110EH, Microfluidics Corp, USA) by one pass through large chambers (400 μm and 200 μm, 800 bar) and four passes through smaller chambers (200 µm and 100 µm, 1600 bar) to produce a CNF gel with a dry content of ~10 g L⁻¹. The total charge of CNFs was determined by conductometric titration as 770 μ mol g⁻¹. CNF dispersions (~2 g L⁻¹) were prepared by Ultra Turrax homogenization, tip sonication, and centrifugation by dilution in milliQ water. The final dry content was determined gravimetrically by drying the dispersion overnight in an oven at 105 °C and cooling down in a desiccator. The measurements were performed in triplicate.

Preparation of cellulose nanopapers

Phosphate buffer was prepared with a 1:1 molar ratio of $\rm K_3PO_4$ and $\rm K_2HPO_4$ in milliQ water. The polymeric nanoparticles were diluted to 0.2 wt% in 10 mM phosphate buffer. The TO-CNF dispersion was diluted to 0.2 wt% (2 g L⁻¹) and the nanoparticle dispersion was added dropwise. The hybrid dispersion was stirred for 30 minutes, and then vacuum filtered over a PVDF membrane (Durapore hydrophilic PVDF Membrane, DVPP Millipore) in analogy to previous studies. The wet cakes were dried for 2 days in holders to prevent buckling in a room conditioned to 50% relative humidity.

Characterization

Nuclear magnetic resonance (NMR) was performed using a Bruker Advance NMR at 400 MHz.

Size exclusion chromatography (SEC) was performed using a SECurity 1260 (Polymer Standard Services, PSS, Mainz, Germany) equipped with an Agilent RID G1362A refractive index detector, an Agilent 1260 VWD VL G1314B UV detector (280 nm) and three columns (PSS Gram 10 μ m; Microguard, 100 Å and 10 000 Å; Analytical). DMSO with 0.5 wt% LiBr was used as the mobile phase at a flow rate of 0.5 ml min $^{-1}$. Calibration was performed using narrow PMMA standards from PSS, ranging from 100 to 1 000 000 g mol $^{-1}$.

Fourier-transform infrared (FTIR) spectroscopy was performed using a PerkinElmer Spectrum 2000 FT-IR equipped with a MKII Golden Gate single reflection AFR system (from Specac Ltd, London, UK) with a MKII heated diamond 45° ATR top plate.

Differential scanning calorimetry (DSC) was performed using a Mettler Toledo DSC. The polymer was freeze-dried and stored in a vacuum oven at 50 °C prior to analysis to avoid excessive moisture in the sample. The polymers were analyzed

at a heating and cooling rate of 10 °C min⁻¹ under a nitrogen atmosphere. The first heating cycle heats to 150 °C and then -50 °C. The second heating cycle was run from -50 to 200 °C and this was used to evaluate the glass transition temperature (T_g). For the OEGMA-containing samples, the minimum temperature was decreased to -80 °C.

Dynamic light scattering (DLS). The hydrodynamic diameter $(D_{\rm H})$, polydispersity index (PDI), and zeta potential (ζ) of the polymeric nanoparticles were determined using a Malvern Zetasizer NanoZS at 0.1 wt% in distilled water or phosphate buffer at 25 °C. The standard for size correlation was polystyrene latex.

Preparation of ultrathin films on QCM-D sensors. An ultrathin film of TO-CNFs was prepared on a SiO₂-coated QCM-D sensor (Biolin Scientific, Gothenburg) by spin-coating a 0.1 wt% TO-CNF suspension. Prior to spin-coating, an anchoring layer of polyethylenimine was applied to the sensor surface. Following TO-CNF deposition, the sensors were heat-treated at 80 °C for 10 minutes. Film uniformity was verified by scanning three different areas using atomic force microscopy (Bruker Multimode 8). The films were stored in a desiccator until use.

Quartz crystal microbalance with dissipation (QCM-D) studies were performed using a QCM-D instrument (E4, Biolin Scientific, Gothenburg, Sweden) to assess the interaction of nanoparticles with TO-CNF surfaces. TO-CNF films were equilibrated in 2.5 mM phosphate buffer, and a stable baseline was established. Nanoparticle dispersions (2 g L $^{-1}$ in 2.5 mM phosphate buffer) were then introduced into the flow cells at 25 °C at a flow rate of 100 μL min $^{-1}$. Following the adsorption phase, the buffer solution was reintroduced to evaluate the reversibility of the interactions. The films after adsorption were imaged with AFM to characterize morphological changes.

Field-emission scanning electron microscopy (FE-SEM) was performed using a Hitachi S-4800. The nanoparticles were mounted on plasma-treated silicon wafer by casting of a 0.01 wt% dispersion. The samples were dried under ambient conditions and coated with a thin layer of Pt/Pd before imaging. The nanopapers were cut with a scalpel, or fractured in the tensile rig before mounting with conducting tape on SEM stubs. The samples were dried in a desiccator and coated with a thin layer of Pt/Pd before imaging. Typical parameters for imaging were 1 keV, 2–5 μA and a working distance of 1.5 mm. The sizes of nanoparticles were measured manually using ImageJ software.

Polymer shell thickness assessment

The thickness of the shell was assessed by taking the difference between $D_{\rm H}$ and $D_{\rm SEM}$ according to eqn (2).

$$t_{\text{shell}} = (D_{\text{H}} - D_{\text{SEM}})/2 \tag{2}$$

Tensile testing was performed using an Instron 5944 with a 500 N load cell at 23 °C and 50% RH. Strips were cut with a punch cutter tool to 6 mm in width, and stored under the

same conditions for at least 48 h prior to testing. The gauge length was set to 30 mm and the strain at 10% min⁻¹. A minimum of 5 specimens per sample were tested.

Results and discussion

Synthesis and characterization of well-defined colloidal nanoparticles

Colloidally stable polymeric nanoparticles were synthesized according to the principles of polymerization-induced self-assembly (PISA) (Fig. 1a). The objective of this study was to

synthesize nanoparticles with different shell functionalities: anionic, polyethylene glycol (PEG) (ether-rich), and glycerol functional (hydroxyl-rich).

First, the water-soluble oligomeric segment stabilizing the surface of the nanoparticles, also called the macromolecular chain-transfer agent (macroCTA), was synthesized *via* reversible addition-fragmentation chain-transfer (RAFT) radical polymerization (Fig. 1ai). Then, the macroCTA was chain extended with the hydrophobic monomer MMA under aqueous conditions (Fig. 1aii). At a certain chain length, this amphiphilic block copolymer self-assembles into monomerswollen micellar structures (Fig. 1aiii). The subsequent conver-

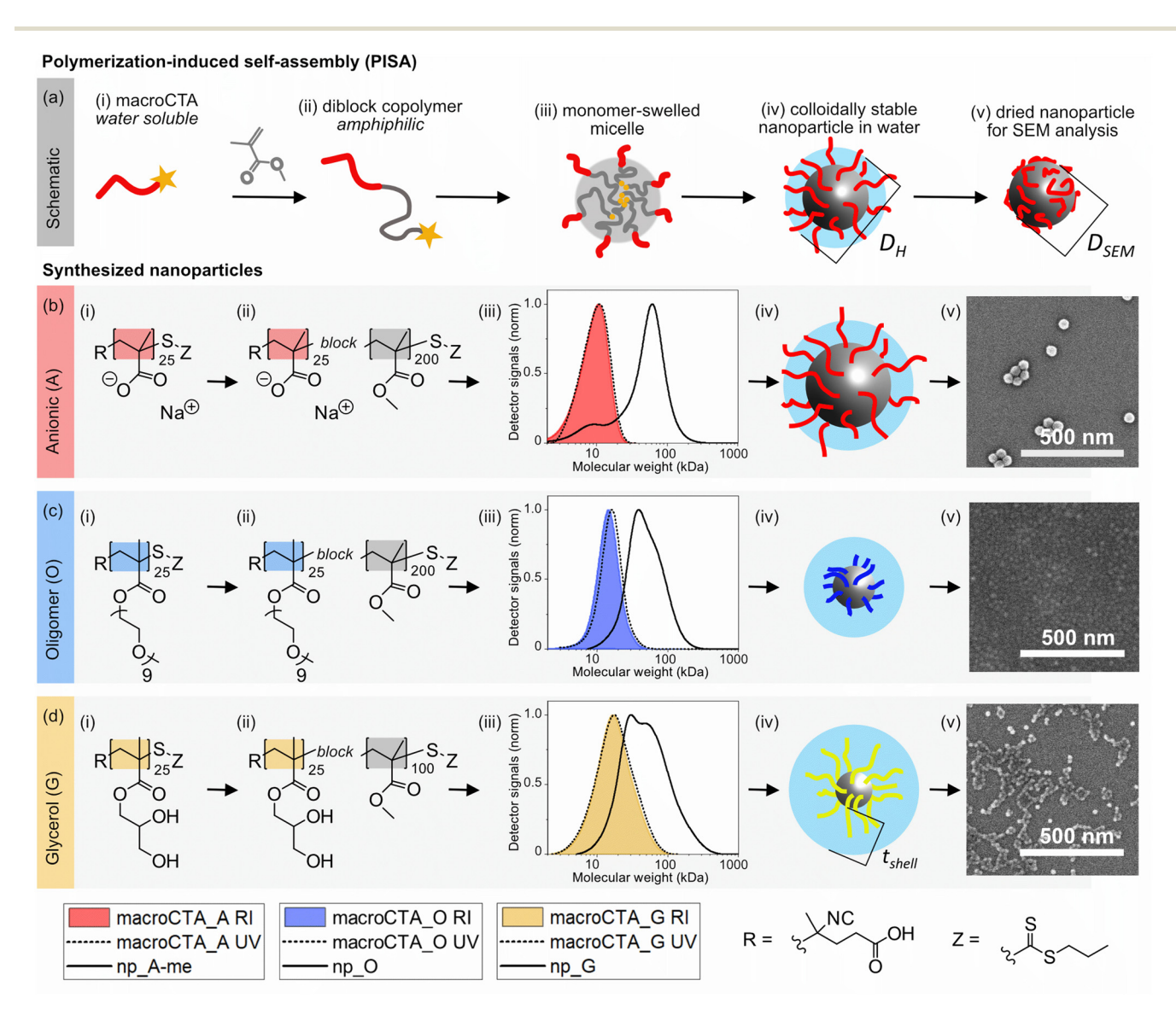


Fig. 1 (a) Schematic of polymerization-induced self-assembly (PISA), where (i) a water-soluble macroCTA is synthesized, which is (ii) chain extended under aqueous conditions with methyl methacrylate (MMA). (iii) The amphiphilic block copolymer self-assembles into a monomer-swollen micelle, and then complete polymerization into (iv) a colloidally stable core-shell nanoparticle occurs. (v) The nanoparticles are dried for visualization in field-emission scanning electron microscopy (SEM). (b) Anionic nanoparticles are synthesized with (bi) a macroCTA of poly(methacrylic acid) and (bii) a chain extended to an amphiphilic block copolymer. (biii) Size-exclusion chromatography (SEC) chromatograms showing the polymer size and distribution of the macroCTA in the refractive index (RI) for concentration and UV detection showing the attachment of the Z group along the distribution, as well as the block copolymer np_A. (biv) Schematic showing the nanoparticle np_A with D_H and D_{SEM} and (v) SEM micrograph of the dried np_A. (c) Structure and characterization of PEG-functional macroCTA_O and np_O, and (d) macroCTA_G and np_G.

Nanoscale

sion of monomer occurs inside the micelles, and results in spherical, colloidally stable, and core-shell nanoparticles with a tailorable shell functionality (Fig. 1aiv). In an aqueous dispersion, these nanoparticles have a water-swelled shell consisting of a hydrophilic polymer with associated water and counter ions. The wet size was assessed through DLS, giving the hydrodynamic diameter DH, as visualized by blue spheres (Fig. 1aiv). The dry size was determined through SEM imaging, giving an evaluation of hydrophobic core size, as visualized by gray spheres (Fig. 1av).

Synthesis and characterization of macroCTA - the stabilizing block

All macroCTAs were synthesized in solution polymerization using thermally initiated RAFT, with a target degree of polymerization (DP) of 25. The RAFT agent 4-cyano-4-[(thiothiopropyl)sulfanyl] pentanoic acid (CTPPA) proves efficient for aqueous PISA and was employed along with an azo-radical initiator. The anionic macroCTA (macroCTA_A) (Fig. 1bi) was synthesized from methacrylic acid (MAA) in water according to the literature procedure.21 CTPPA has poor water solubility, and was dissolved in the monomer before addition to the aqueous phase. This formed a cloudy heterogeneous monoglycerol methacrylate (GMA) solution. The GMA solution was polymerized using CTPPA and thermal RAFT. The polymer system became homogeneous as the temperature increased. The PEG-functional macroCTA (macroCTA_O) (Fig. 1ci) was synthesized from oligo(ethylene glycol) methyl ether methacrylate (OEGMA), a monomer known for its use in polymers with water solubility and thermosensitivity.²³ Polymers containing OEGMA exhibit aqueous lower- and upper critical solution temperatures (LCST and UCST) and thus macroCTA_O was synthesized in 1,4-dioxane to avoid solubility issues. The glycerol-functional macroCTA (macroCTA_G) (Fig. 1di) was synthesized from glycidyl monomethacrylate according to the literature.²² The commercial glycidyl methacrylate monomer was hydrolyzed in water at 80 °C for 20 hours, producing a monoglycerol methacrylate (GMA) solution. The GMA solution was polymerized using CTPPA and thermal RAFT. The macroCTAs' structures were confirmed using ¹H and ¹³C NMR (Fig. S2, S5 and S8).

Table 1 Characterization of macroCTA

Sample	p (%)	$M_{\rm n~theo}({\rm kDa})$	$M_{\rm n}$ (kDa)	Đ	$T_{\mathrm{g}}\left(^{\circ}\mathrm{C}\right)$
macroCTA_A	95	2.3	4.3	1.38	—
macroCTA_O	97	12.4	15.3	1.17	-46
macroCTA_G	98	4.6	14.7	1.43	97
macroCTA_D³	99	4.2	2.86	1.35	—

Conversion (p) as calculated from ¹H NMR, theoretical molecular weight $(M_{\rm n~theo})$ as calculated from 100% monomer conversion, molecular weight (M_n) and polydispersity (D) as calculated from DMSO-SEC and glass transition temperature (T_g) as calculated from DSC. The cationic macroCTA_D is published elsewhere, and the molecular weights are obtained from SEC in DMF.3

Table 1 summarizes the characterization of macroCTAs produced in this study. The macroCTAs have reasonably low polydispersities (D) and number average molecular weight (M_n) values slightly larger than the theoretical values $(M_{\rm n-theo})$. MacroCTA_O has the lowest D value of 1.17 and the M_n value is close to the theoretical value, suggesting good RAFT control. MacroCTA_A and macroCTA_G have higher D values and M_n values significantly larger than the theoretical values. This may be due to the poor solubility of CTPPA, which results in a lower true concentration of CTPPA than targeted and thus a larger molecular weight. Table 1 also contains information on a cationic macroCTA synthesized from N,N-dimethylamino ethyl methacrylate (DMAEMA), also with a target DP of 25, for reference.3 The presence of the trithiocarbonate moiety, which is necessary for chain extension, was confirmed over the full polymer distribution for all macroCTAs using an SEC UV detector at 280 nm (Fig. 1b-diii), showing that all macroCTAs are suitable for chain extension via PISA.

The glass transition temperatures (T_g) found for these macroCTAs by differential scanning calorimetry are similar to those expected from the literature. For macroCTA_A, the expected $T_{\rm g}$ is higher than the degradation temperature, extrapolated to 230 °C, 24 and thus no T_g was found in the range -50-200 °C. The $T_{\rm g}$ values of macroCTA_G and macroCTA_O were 97 and -46 °C, similar to the data in the literature. 23,25 These results suggest that the lengths of the macroCTA blocks, although short, are sufficiently close to the entanglement molecular weight M_e to produce glass transition temperatures similar to those of high molecular weight polymers.

Synthesis and characterization of colloidal nanoparticles via RAFT-PISA

The purified macroCTAs were dissolved in water and chain extended with MMA in emulsion polymerization, producing block copolymer structures (Fig. 1b-dii). The block copolymers and resulting nanoparticles are termed np_A, np_O and np_G for nanoparticles with surfaces consisting of anions, PEG, and glycerol, respectively. The monomer conversions, evaluated gravimetrically, were all above 80%. Table 2 shows the characteristics of the block copolymers and nanoparticles, as well as cationic nanoparticles produced with macroCTA_D (Table 1), as published elsewhere.3

The successful chain extension with MMA was confirmed by SEC (Fig. 1b-diii), showing the reasonable D and M_n values of all nanoparticles (Table 2). The high molecular weight shoulders in np_O and np_G suggest termination events due to cross-coupling, which is common at high monomer conversion. The dispersity of np_A is rather high, stemming from a significant low molecular weight shoulder (Fig. 1biii). This shoulder likely appears due to trithiocarbonate hydrolysis under these conditions, as shown by Chaduc et al., which leads to generation of dead chains and thus poor blocking efficiency.²⁶

The block copolymer monomer ratios were confirmed by ¹H NMR as detailed in the SI (Fig. S9 and S10).

The polymers were formulated to yield nanoparticles with similar hydrodynamic diameters (D_H) (Table 2). The anionic

 Table 2
 Characterization of block copolymer nanoparticles

Sample	$M_{\rm n~theo}({\rm kDa})$	$M_{\rm n}$ (kDa)	Đ	T_{g} (°C)	$D_{\rm H}$ (nm)	PDI	ζ (mV)	D_{SEM} (nm)	$t_{ m shell}$ (nm)	Shell (wt%)
np_A	22.5	26.5	2.12	—; 127	70 ± 0.3	0.02	-64 ± 0.2	46 ± 7	12	10
np_O	32.8	41.0	1.37	-45;126	54 ± 0.2	0.13	-35 ± 0.3	23 ± 4	16	38
np_G	14.7	37.1	1.79	63; 120	70 ± 0.8	0.20	-50 ± 3.2	20 ± 3	25	29
np_D_S	24.2	34.7	2.49	NA	40 ± 0.1	0.08	54 ± 3.3	26 ± 5	7	16
$\mathrm{np}_D_{\mathrm{L}}$	54.2	392	1.82	NA	119 ± 0.1	0.03	66 ± 0.2	79 ± 13	20	7

Theoretical molecular weight $(M_{\rm n})$ assuming 100% monomer conversion, molecular weight $(M_{\rm n})$ and dispersity (D) obtained from DMSO-SEC, glass transition temperature $(T_{\rm g})$ obtained from DSC, hydrodynamic diameter $(D_{\rm H})$, size polydispersity (PDI) and zeta potential (ζ) obtained from DLS, and core size $(D_{\rm SEM})$ obtained from FE-SEM imaging. The shell thickness was calculated from the difference between $D_{\rm H}$ and $D_{\rm SEM}$, and assumes that the PMMA core does not swell. Np_A was methylated before SEC, and the molecular weights of $D_{\rm L}$ and $D_{\rm S}$ were obtained from SEC in DMF.³

macroCTA_A yielded nanoparticles with a very low PDI when synthesized at pH 5.5, due to the charged nature of the macroCTA. This is evidenced by a significantly increased PDI value when PISA was performed at pH 3.5 where macroCTA_A will be mostly non-charged (Fig. S12). MacroCTA_O and macroCTA G vielded nanoparticles (np O and np G) with a somewhat wider size distribution (PDI < 0.2). These PDI values are similar to what is found in the literature for these systems, and the nanoparticles can still be considered quite monomodal in size.^{22,26} All nanoparticles show negative zeta potentials (ζ) . For np_O and np_G, the negative ζ stems from the R-group (Fig. 1), which means that every polymer chain has a terminal carboxylic acid group protruding from the nanoparticle surface. The use of CTAs bearing carboxylic-functional R-groups has been shown to enhance the stability of PISA nanoparticles formed with non-charged blocks.²⁷

SEM imaging shows the diameter of the dried nanoparticles $(D_{\rm SEM})$, which can be interpreted as the size of the rigid MMA core as the water-soluble shell polymer collapses into a very thin layer under high-vacuum conditions (Fig. 1a–dv). The difference between the $D_{\rm H}$ and $D_{\rm SEM}$ values thus gives an indication of the hydrated shell thickness (Table 2, $t_{\rm shell}$ (nm)) (Fig. 1div). The anionic nanoparticles have a hydrated shell of \sim 12 nm, which is similar to those of charged cationic nanoparticles $D_{\rm L}$ and $D_{\rm S}$ (Table 2).³

The glycerol- and PEG-functional nanoparticles (np_G and np_O, respectively) show much larger size differences in wet and dry states. PEG is well known for binding water strongly, and a large amount of associated water on the nanoparticle surface could lead to these results. Another hypothesis for the observed results could be if the macroCTA_O block leads to swelling of the outer part of the PMMA core through mixing of the polymer blocks. The two T_g values found for np_O are, however, similar to the expected T_g values of each block, showing that the polymer blocks are immiscible when no water is present.

The glycerol functional nanoparticles, np_G, show the largest difference between the wet and dry sizes. It is possible that macroCTA_G is actually longer than DP 25, as evidenced by the high molecular weight (Table 1). Based on the assessed molecular weight M_n , the macroCTA_G block could be up to 15 nm

in length when fully extended, but the shell thickness of these nanoparticles was estimated to be 25 nm. It is also possible that the adjacent macroCTA_G block allows for water to penetrate into the PMMA core, as hypothesized in np_O. The measured $T_{\rm g}$ values of np_G indicate a pure PMMA segment with high glass transition and purity. The $T_{\rm g}$ of macroCTA_G, however, decreased when attached to the block copolymer MMA segment. Usually, the opposite effect would be expected when there is significant miscibility between polymer segments. It is possible that macroCTA_G is not able to fully hydrogen bond with other similar segments, due to the attached MMA segment or the attachment to the surface of the nanoparticles.

The nanoparticles were later diluted in phosphate buffer to produce cellulose nanopapers, and thus their $D_{\rm H}$ and ζ values were determined under these conditions. All three nanoparticles show a slight reduction in the $D_{\rm H}$ value at the maximum total buffer (2.5 mM), and a reduction in the ζ value (Fig. S13). This shows that the nanoparticles tend to contract with the addition of buffer, but that they are still colloidally stable at the ionic strengths utilized.

Fig. 1a–div show schematics of the synthesized nanoparticles, with $D_{\rm H}$ and $D_{\rm SEM}$ indicated by blue and grey spheres, respectively. This section details the synthesis of monodisperse colloidally stable nanoparticles with a rigid PMMA core and different water-soluble polymeric stabilizing segments on their surface.

Interactions of the nanoparticles of different shell functionalities with TO-CNFs

To investigate whether nanoparticles with different functionalities interact with or adsorb to TO-CNFs, quartz crystal microbalance with dissipation monitoring (QCM-D) was performed. QCM-D has previously shown that cationic nanoparticles with PDMAEMA-functional shells, such as np_D_S and np_D_L (Table 2), interact strongly with anionic TO-CNFs and lead to irreversible adsorption. TO-CNFs were spin-coated onto quartz crystals to produce films with good surface coverage and low roughness (Fig. 2d). QCM-D was performed in 2.5 mM phosphate buffer to mimic the conditions in nanopaper fabrication.

Fig. 2a-c show representative QCM-D curves of the interaction of different nanoparticles with TO-CNF ultrathin films.

Nanoscale Paper (a) QCM-D with np A (b) QCM-D with np O (c) QCM-D with np G

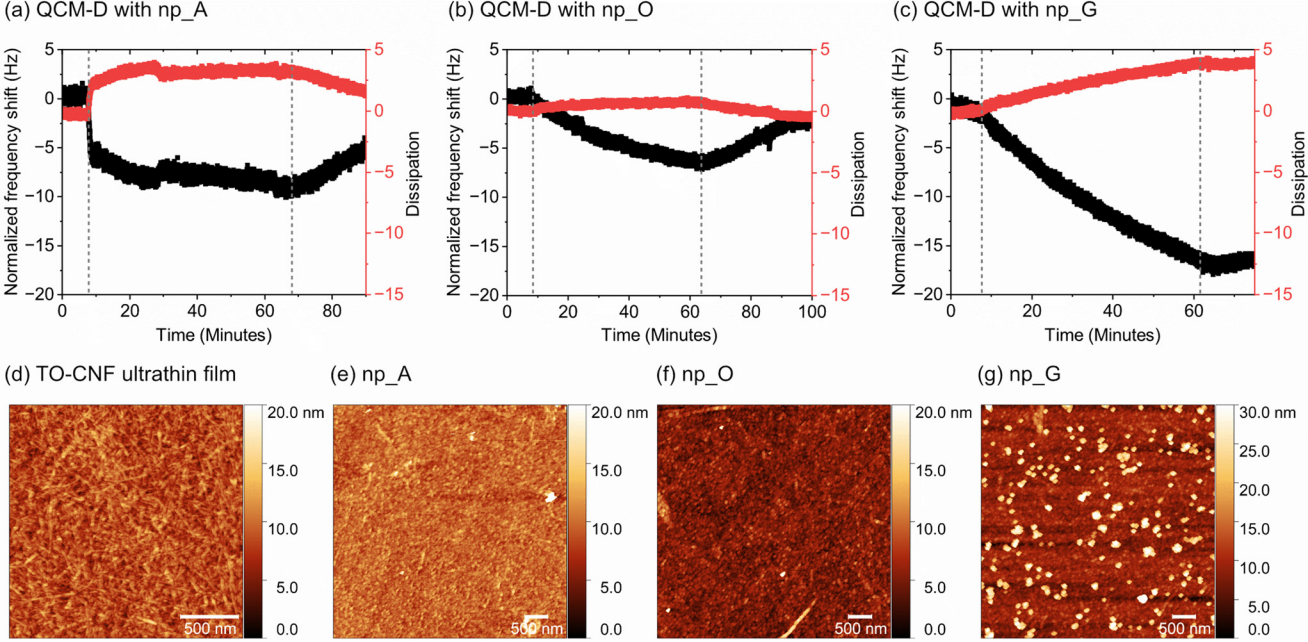


Fig. 2 Quartz crystal microbalance with dissipation monitoring (QCM-D) of nanoparticles on the anionic TO-CNF model surfaces. (a) np_A and (b) np_O show slight adsorption and reversibility, whereas (c) np_G shows more significant adsorption and a certain irreversibility. AFM images of (d) the TO-CNF model surface used for adsorption experiments and surfaces after the QCM-D and washing step of (e) np_A, (f) np_O and (g) np_G.

Upon injection of the nanoparticles, the frequency shifted to negative values, indicating the interaction of nanoparticles with TO-CNF surfaces. However, in the case of np_A and np_O, the magnitude of the frequency shift was minimal, especially considering the bulk contribution; it can be concluded that there was no considerable interaction of these nanoparticles with TO-CNF surfaces. Furthermore, when the system was rinsed with buffer, the frequency values were reverted to the original baseline. This indicates that any interactions that may have occurred were likely weak and reversible. The reversibility of these adsorptions was further confirmed by AFM, where no nanoparticles can be observed after the rinsing step (Fig. 2e and f).

Interestingly, in the case of np_G, the frequency shift was much larger compared to those of np_A and np_O. Moreover, upon rinsing, the frequency did not shift towards the baseline, indicating the irreversibility of interaction of np_G particles with TO-CNF surfaces. The adsorbed np_G nanoparticles and their aggregates were visible in the AFM micrograph of TO-CNF films after the washing step (Fig. 2g). The height measurement in Fig. 2g shows that the nanoparticles are ~20 nm in size, similar to the sizes seen in the SEM (Fig. 1dv and Table 2). In the xy-plane, nanoparticles of 50-60 nm size formed into larger aggregates are seen. The increased size of nanoparticles from this perspective may indicate that they lose their spherical shape upon adsorption. What is clear, however, is that np_G adsorbs and aggregates upon contact with TO-CNF model surfaces, which is not the case for np_A or np_O. This indicates the affinity between np_G and TO-CNFs under aqueous conditions.

Fabrication of hybrid cellulose nanopapers

Fig. 3 schematically shows the process of producing hybrid cellulose nanopapers with PISA nanoparticles. A dispersion of carboxylate-functional cellulose nanofibrils (TO-CNFs) was produced via TEMPO-mediated oxidation. The material was homogenized and sonicated to achieve high fibrillation and separation between nanoscopic fibrils. The dispersion at 0.2 wt% (2 g L⁻¹) in milliQ water is free-flowing, but at this concentration, there are still significant fibril overlaps and fibril-fibril interactions (Fig. 3a).30 The colloidally stable polymeric nanoparticles were diluted to 0.2 wt% in 10 mM phosphate buffer or in milliQ water, and were then added to the CNF dispersion under vigorous stirring before vacuum filtering to transparent films with a target thickness of 40 µm (Fig. 3b-d). The buffer was added when hybridizing anionic TO-CNFs with oppositely charged nanoparticles to avoid macroscopic aggregation.^{5,6} In this work, we not only use the same buffer, but also investigate the removal of the buffer completely from the system.

Nanoparticle additives act as retention aids in vacuum filtration

The filtrate water was collected and freeze-dried. The filtrates are termed filt_np_w, where np is the nanoparticle additive A, O, or G and w is the nanoparticle amount in wt%. Gravimetric analysis and FTIR showed that in the TO-CNF reference, a significant amount (>30%) of cellulose was lost through the pores of the filter (Fig. 4a and b). The addition of nanoparticles reduced the material loss, both when buffer was added and when it was not (Fig. 4a and b). This indicates that there is

Paper Nanoscale

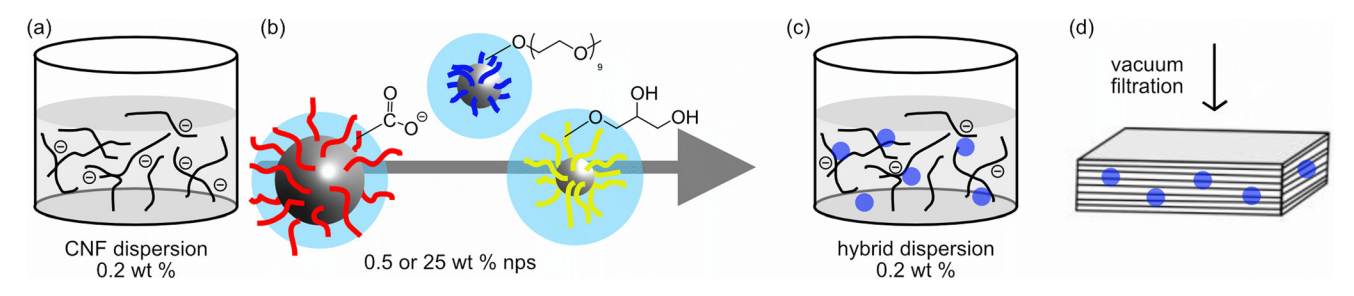


Fig. 3 Schematic showing the fabrication of nanocomposite materials. (a) A dispersion of cellulose nanofibrils (CNFs) at 0.2 wt%. (b) Polymeric nanoparticles are added from a 0.2 wt% dispersion to create (c) a hybrid dispersion with 0–25 wt% polymeric nanoparticles to cellulose. (d) This hybrid dispersion is vacuum filtered and dried to form cellulose-rich nanocomposite materials.

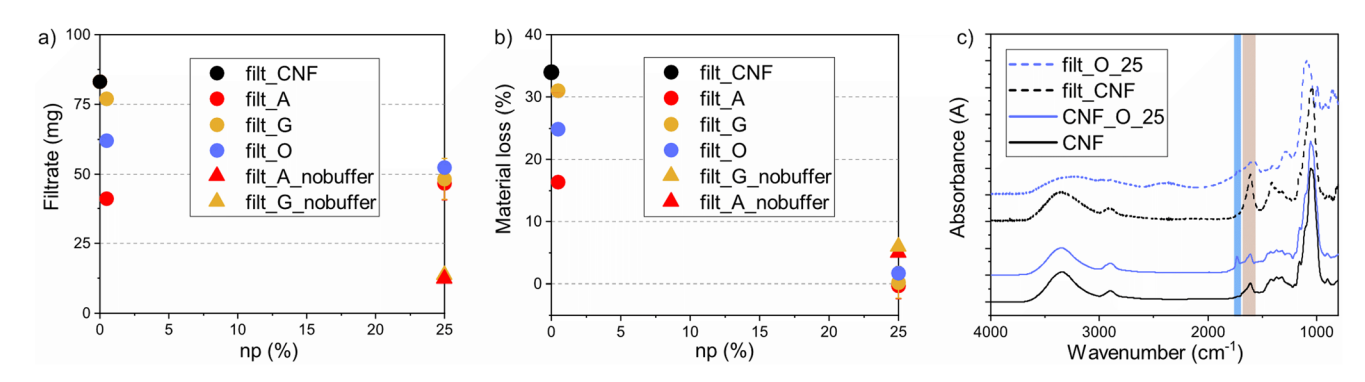


Fig. 4 (a) The filtrate mass lost during vacuum filtration and (b) percentage material loss show that the polymeric nanoparticles act as retention aids for the CNFs. (c) The filtrate consists of CNFs and nanoparticles, but fewer nanoparticles than in the finished film, indicating that the CNFs are lost at a higher rate than the nanoparticles, which are instead retained in the dried material.

some interaction between the TO-CNFs and the nanoparticles already in the dispersion phase. Although the QCM-D results showed slight adsorption, it was surprising that the effect was so large. Even at 0.5 wt% addition, PISA nanoparticles acted as retention aids where they led to reduced loss of TO-CNFs through the filter.

FTIR analysis of the filtrate shows that both the TO-CNFs and the nanoparticles passed through the filter (Fig. 4c and Fig. S15). These components could be qualitatively assessed by the signals at 1620 cm⁻¹ (C-O-C group of TO-CNFs) and 1730 cm⁻¹ (carbonyl group of nanoparticles). As compared to the FTIR spectra of the nanopapers, the filtrate appeared to contain fewer nanoparticles than TO-CNFs (Fig. 4c). Again, this indicated that the nanoparticles act as retention aids in the TO-CNF matrix. This means that the nanopapers may contain a slightly higher weight percentage of nanoparticles than what was added in the hybrid dispersion.

Nanoparticle additives are well dispersed in the CNF matrix

The cellulose-rich dry materials are termed CNF_np_w, where np is the type of nanoparticle additive and w is the nanoparticle amount in wt%. The materials were imaged on the surface and in the cross-section (Fig. 5). The surfaces showed small amounts of nanoparticles at 0.5 wt% and a more extensive surface coverage at 25 wt% as expected. In some regions, it could also be seen that the cellulose matrix was distorted by

a nanoparticle lying underneath the surface (CNF_A_0.5, Fig. 5c, arrow (i)). These effects were easiest to see with np_A because it has the largest core size. In general, the surfaces of all nanopapers were smooth, and no nanoparticle aggregates were apparent.

The fracture surfaces showed that the nanoparticles were distributed throughout the bulk of the material. In CNF_A_25, spheres were observable throughout the cross-section (Fig. 5d, arrow (ii)). With the other nanoparticles, observation of spheres became more challenging because of their size and the difficulties of imaging a rough surface at high magnification. However, it could be concluded that the incorporation of all nanoparticles at both 0.5 and 25 wt% induced changes in material structure throughout the cross-section, as compared to the TO-CNF reference (Fig. 5b). The nanoparticles were thus present throughout the material, and not only at the surface.

Mechanical properties of hybrid nanopapers

The nanopapers were cut into strips and tensile tested in a standard tensile rig set-up. Each sample was tested with a minimum of five specimens. The elastic, yielding, and plastic behaviors of each material were reproducible, as apparent in Fig. S16. However, the tensile strength was more variable due to the brittle nature of fracture events. This resulted in significant scatter in strain to failure and toughness (area under the

Nanoscale

a)
c) CNF_A_0.5
e) CNF_O_0.5
g) CNF_G_0.5

b) CNF

d) CNF_A_25
f) CNF_O_25
h) CNF_G_25

Fig. 5 Cross-sections (fracture surfaces, left) and surface morphologies (right) of the hybrid nanopapers. (a) Directions imaged in the nanopapers, (b) reference with only CNFs, (c and d) with np_A, (e and f) with np_G, and (g and h) with np_O. The images show changes in the cross-sectional structures upon the incorporation of nanoparticles, indicating that the nanoparticles are distributed throughout the CNF matrix. The arrows show (i) the nanoparticles embedded in the TO-CNF matrix and (ii) the nanoparticles in the cross-section. Scale bar: 500 nm.

stress-strain curve) (Fig. S17). This is typical behavior for many cellulose nanopaper films, since failure is often brittle.³¹

The addition of 25 wt% polymeric nanoparticles led to a reduction in the Young's modulus (E) and slope in the plastic region (n), but increased strain to failure (Fig. 6a, b and

Fig. S17). The nanoparticles improve ductility, but what is the role of the shell properties in modification effects? The extracted values for E and n showed weak dependency on the nanoparticle surface. When looking closer at the data, there was an effect on the yield strength (Fig. 6a). Np_A and np_G

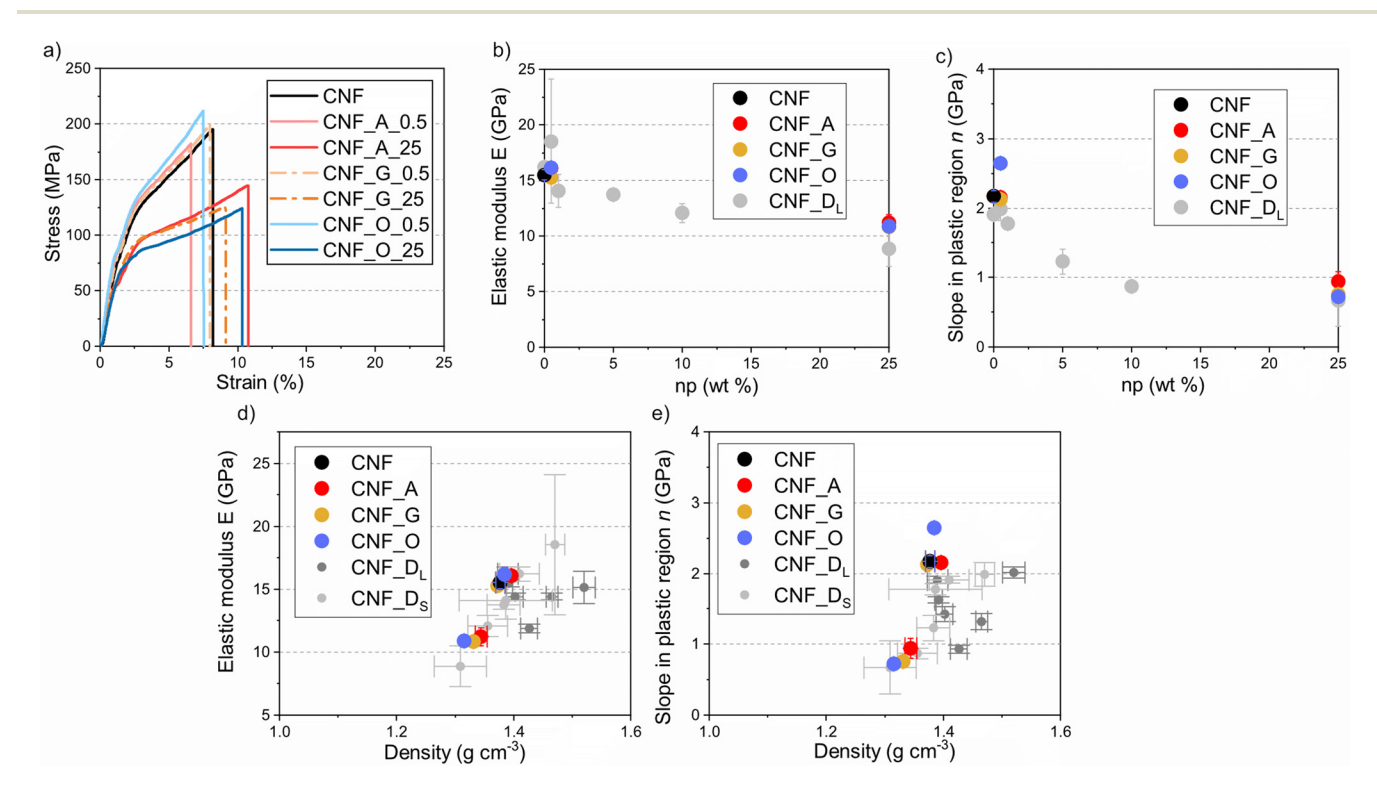


Fig. 6 Tensile properties of hybrid cellulose nanopapers. (a) Representative stress—strain curves of all materials made with buffer, (b) Young's moduli (E) of all materials, and (c) slope in the plastic region (n) of all materials. The dependency of mechanical properties not only on density, but also on nanoparticle functionality. (a) E and (b) n.

Paper Nanoscale

gave rise to very similar yield behavior, but np_O reduced the yield strength. The yield behavior was reproducible, as apparent in the data in Fig. S16.

The addition of very small amounts of nanoparticles (0.5 wt%) has been previously shown to lead to subtle but reproducible increases in E and n.³ The work used cationic polymeric nanoparticles D_L and D_S, as detailed in Table 2, and the hypothesis was that the cationic shell polymer dehydrates CNFs through electrostatic interactions, increasing the density, the packing of CNFs and mechanical properties. Although the effect was small, similar behavior was apparent with np O in its effect on n, whereas np A and np G did not increase n. The stress-strain curves in Fig. 6a show that CNF_O_0.5 deviates from the behavior of CNF_A_0.5 and CNF_G_0.5.

Factors controlling mechanical properties in hybrid nanopapers

In nanocomposites with TO-CNFs as the "continuous" binder phase, an increased density of the TO-CNF phase is expected to have an effect on the mechanical properties by reducing the nanoporosity and improving the CNF-CNF interfibril bonding.32,33 We have previously shown that cationic additives can increase or decrease the sheet density, where E and n are positively dependent on density³ (Fig. 6d, e, CNF_ D_L and CNF_D_S). This is surprising, as nanoparticles have lower density than TO-CNFs and their incorporation would be assumed to decrease the composite density. For the present data, there is also an effect from increased density (Fig. 6d and e) as in previous studies. Small amounts (0.5 wt%) of the nanoparticles in this study increased the density very slightly, with an associated subtle increase in n. Higher amounts (25 wt%) led to decreased density, as the nanoparticles have lower density than TO-CNFs. The reduced yield stress and increased strain-to-failure with 25 wt% nanoparticles are likely to be a consequence of reduced CNF interfibril bonding due to the nanoparticles. These nanoparticles can thus be used to modify the mechanical response of nanopapers.

This study hypothesized that the nanoparticle-CNF interface governs mechanical properties through a slipping mechanism. The results acquired in this work show that the effect of nanoparticle surface functionality is subtle. Previous work has shown that the surface of spherical particles impacts interactions and bulk material behavior when nanocellulose is the minority component. Mattos et al. showed that the surface hydrophobicity of silica particles impacts the mechanical response in nanocellulose hybrids.34 Similarly, Leiner et al. showed that the introduction of hydroxy-functional moieties onto the shell of polymeric core-shell particles improves adhesion with cellulose nanowhiskers, and subsequently impacts the mechanical and optical properties of such hybrids.³⁵ Such effects are not observed in the present work, and this might be due to the relatively low amounts of nanoparticles vs. CNFs in the materials fabricated. This is associated with the large surface area of TO-CNFs, which means that

at 25 wt% nanoparticles, a maximum of 10% of the CNF area is covered by the nanoparticles (Fig. S18, CNF_G_25). The materials fabricated in this work are thus dominated by strong fibril-fibril bonds in the dry state, and not by the fibril-nanoparticle interface.

Conclusions

In this study, polymeric nanoparticles with a rigid core and different shell functionalities were successfully synthesized via RAFT-PISA. The shells of the nanoparticles were synthesized with anionic, PEG-like, or hydroxyl-rich functionalities to study the influence on cellulose interactions and effects on the mechanical behavior of cellulose nanopapers. The nature of the nanoparticle shell governs the adsorption behavior to TO-CNFs, with the hydroxyl-functional nanoparticles showing stronger affinity than the anionic and PEG-functional nanoparticles. All the nanoparticles studied act as retention aid additives in the production of cellulose nanopapers, with little effect of the surface functionality.

Mechanical testing revealed that low amounts of nanoparticles (0.5 wt%) have a small influence on mechanical behavior. The presence of 25 wt% nanoparticles modifies deformation mechanisms in the TO-CNF phase, so that yielding takes place at lower global stress and strain-to-failure is increased. This can be used to tailor the stress-strain response of the composites. One may note that modification of thin TO-CNF films using glassy polymer particles requires nanoscale particle size. An advantage of using glassy polymer nanoparticles is that the sacrifice in Young's modulus is relatively minor, compared to modification with rubbery particles. The present work also shows that the effect of particle surface functionality on mechanical behavior is minor. This is an important insight for designing nanocomposites from CNFs and polymeric particles.

Overall, this work offers mechanistic insights into how nanoparticle surface design affects hybrid, CNF-rich materials, supporting the development of tunable, water-processed nanostructures for sustainable applications.

Author contributions

Å. J. performed sample preparation, carried out most characterization, analysed the data, and drafted and revised the manuscript. K. G. performed sample preparation and revised the manuscript. V. A. performed all QCM-D measurements, analysed the data and revised the manuscript. L. B. and E. M. supervised the project and revised the manuscript. All authors have given approval to the final version of the manuscript.

Conflicts of interest

There are no conflicts of interest to declare.

Nanoscale Paper

Data availability

The data supporting this article have been included as part of the supplementary information (SI). Supplementary information is available. See DOI: https://doi.org/10.1039/d5nr03629a.

Acknowledgements

The authors acknowledge funding from the Swedish Research Council (2020-05486), the Knut and Alice Wallenberg foundation (KAW) through the Wallenberg Wood Science Centre (WWSC) (2018.0452), and FibRe, a "Vinnova-funded Competence Centre for Design for Circularity: Lignocellulose-based Thermoplastics" (2019-00047).

References

- 1 T. Li, C. Chen, A. H. Brozena, J. Y. Zhu, L. Xu, C. Driemeier, J. Dai, O. J. Rojas, A. Isogai, L. Wågberg and L. Hu, Developing fibrillated cellulose as a sustainable technological material, *Nature*, 2021, **590**, 47–56, DOI: 10.1038/s41586-020-03167-7.
- 2 B. Wang, S. Qiu, Z. Chen, Y. Hu, G. Shi, H. Zhuo, H. Zhang and L. Zhong, Assembling nanocelluloses into fibrous materials and their emerging applications, *Carbohydr. Polym.*, 2023, 299, 120008, DOI: 10.1016/j. carbpol.2022.120008.
- 3 Å. Jerlhagen, K. Gordeyeva, M. Cattaruzza, L. Brandt, B. Sochor, S. Koyiloth Vayalil, S. V. Roth, L. Wågberg and E. Malmström, Decoding in-plane orientation in cellulose nanopapers hybridized with tailored polymeric nanoparticles, *Nanoscale*, 2025, 8712–8723, DOI: 10.1039/D4NR04381B.
- 4 M. Wang, A. Olszewska, A. Walther, J. M. Malho, F. H. Schacher, J. Ruokolainen, M. Ankerfors, J. Laine, L. A. Berglund, M. Osterberg and O. Ikkala, Colloidal ionic assembly between anionic native cellulose nanofibrils and cationic block copolymer micelles into biomimetic nanocomposites, *Biomacromolecules*, 2011, 12, 2074–2081, DOI: 10.1021/bm101561m.
- 5 J. Engström, F. L. Hatton, L. Wågberg, F. D'Agosto, M. Lansalot, E. Malmström and A. Carlmark, Soft and rigid core latex nanoparticles prepared by RAFT-mediated surfactant-free emulsion polymerization for cellulose modification a comparative study, *Polym. Chem.*, 2017, 8, 1061–1073, DOI: 10.1039/c6py01904h.
- 6 A. E. Alexakis, Å. Jerlhagen, M. R. T. Leggieri, A. Eliasson, T. Benselfelt and E. Malmström, Modification of CNF-Networks by the Addition of Small Amounts of Well-Defined Rigid Cationic Nanolatexes, *Macromol. Chem. Phys.*, 2023, 224, 2200249, DOI: 10.1002/macp.202200249.
- 7 L. Carlsson, A. Fall, I. Chaduc, L. Wågberg, B. Charleux, E. Malmström, F. D'Agosto, M. Lansalot and A. Carlmark,

- Modification of cellulose model surfaces by cationic polymer latexes prepared by RAFT-mediated surfactant-free emulsion polymerization, *Polym. Chem.*, 2014, 5, 6076–6086, DOI: 10.1039/c4py00675e.
- 8 K. Larsson, L. A. Berglund, M. Ankerfors and T. Lindström, Polylactide latex/nanofibrillated cellulose bionanocomposites of high nanofibrillated cellulose content and nanopaper network structure prepared by a papermaking route, *J. Appl. Polym. Sci.*, 2012, 125, 2460–2466, DOI: 10.1002/app.36413.
- 9 T. Kaldéus, M. R. Telaretti Leggieri, C. Cobo Sanchez and E. Malmström, All-Aqueous SI-ARGET ATRP from Cellulose Nanofibrils Using Hydrophilic and Hydrophobic Monomers, *Biomacromolecules*, 2019, **20**, 1937–1943, DOI: 10.1021/acs.biomac.9b00153.
- 10 E. Malmström and A. Carlmark, Controlled grafting of cellulose fibres – an outlook beyond paper and cardboard, *Polym. Chem.*, 2012, 3(7), 1702–1713, DOI: 10.1039/ c1pv00445i.
- 11 V. Arumughan, T. Nypelö, M. Hasani and A. Larsson, Fundamental aspects of the non-covalent modification of cellulose via polymer adsorption, *Adv. Colloid Interface Sci.*, 2021, 298, 102529, DOI: 10.1016/j.cis.2021.102529.
- 12 C. J. Ferguson, R. J. Hughes, B. T. T. Pham, B. S. Hawkett, R. G. Gilbert, A. K. Serelis and C. H. Such, Effective ab Initio Emulsion Polymerization under RAFT Control, *Macromolecules*, 2002, 35(25), 9243–9245, DOI: 10.1021/ ma025626j.
- 13 F. D'Agosto, J. Rieger and M. Lansalot, RAFT-Mediated Polymerization-Induced Self-Assembly, *Angew. Chem., Int. Ed.*, 2020, **59**, 8368–8392, DOI: 10.1002/anie.201911758.
- 14 A. R. Motezakker, L. G. Greca, E. Boschi, G. Siqueira, F. Lundell, T. Rosén, G. Nyström and L. D. Söderberg, Stick, Slide, or Bounce: Charge Density Controls Nanoparticle Diffusion, ACS Nano, 2024, 18, 28636–28648, DOI: 10.1021/acsnano.4c05077.
- 15 E. Niinivaara and E. D. Cranston, Bottom-up assembly of nanocellulose structures, *Carbohydr. Polym.*, 2020, 247, 116664, DOI: 10.1016/j.carbpol.2020.116664.
- 16 M. Nordenström, T. Benselfelt, R. Hollertz, S. Wennmalm, P. A. Larsson, A. Mehandzhiyski, N. Rolland, I. Zozoulenko, D. Söderberg and L. Wågberg, The structure of cellulose nanofibril networks at low concentrations and their stabilizing action on colloidal particles, *Carbohydr. Polym.*, 2022, 297, 120046, DOI: 10.1016/j.carbpol.2022.120046.
- 17 J. Engström, A. M. Jimenez and E. Malmström, Nanoparticle rearrangement under stress in networks of cellulose nanofibrils using in situ SAXS during tensile testing, *Nanoscale*, 2020, **12**, 6462–6471, DOI: 10.1039/c9nr10964a.
- 18 Å. Jerlhagen, O. Wilson and E. Malmström, Self-Catalyzed Hydrolysis of Nitrile-Containing RAFT Chain-Transfer Agent and Its Impact upon Polymerization Control of Methacrylic Monomers, ACS Macro Lett., 2024, 565–570, DOI: 10.1021/acsmacrolett.4c00112.
- 19 T. Kaldéus, M. Nordenström, A. Carlmark, L. Wågberg and E. Malmström, Insights into the EDC-mediated PEGylation

Paper Nanoscale

- of cellulose nanofibrils and their colloidal stability, Carbohydr. Polym., 2018, 181, 871-878, DOI: 10.1016/j. carbpol.2017.11.065.
- 20 T. Saito, M. Hirota, N. Tamura, S. Kimura, H. Fukuzumi, L. Heux and A. Isogai, Individualization of Nano-Sized Plant Cellulose Fibrils by Direct Surface Carboxylation Using TEMPO Catalyst under Neutral Conditions, Biomacromolecules, 2009, 10(7), 1992–1996, DOI: 10.1021/ bm900414t.
- 21 I. Chaduc, M. Lansalot, F. D'Agosto and B. Charleux, RAFT Polymerization of Methacrylic Acid Macromolecules, 2012, 45(3), 1241-1247, DOI: 10.1021/ ma2023815.
- 22 V. J. Cunningham, A. M. Alswieleh, K. L. Thompson, M. Williams, G. J. Leggett, S. P. Armes and O. M. Musa, Poly(glycerol monomethacrylate)-Poly(benzyl methacrylate) Diblock Copolymer Nanoparticles via RAFT Emulsion Polymerization: Synthesis, Characterization, and Interfacial Activity, Macromolecules, 2014, 47(16), 5613-5623, DOI: 10.1021/ma501140h.
- 23 J. Ramírez, V. Montoya, C. Licea and A. Gónzalez, Tunable Thermo-Responsive Copolymers from DEGMA and OEGMA Synthesized by RAFT Polymerization and the Effect of the Concentration and Saline Phosphate Buffer on its Phase Transition, Polymers, 2019, 11(10), 1657, DOI: 10.3390/ polym11101657.
- 24 J. Kolarík and M. Štol, Relaxation behaviour of poly (methacrylic acid) and its copolymers with 2-hydroxyethyl methacrylate, Polym. J., 1973, 5(2), 158-163.
- 25 C. Ventura-Hunter, V. D. Lechuga-Islas, J. Ulbrich, C. Kellner, U. S. Schubert, E. Saldívar-Guerra, M. Rosales-Guzmán and C. Guerrero-Sánchez, Glycerol methacrylatebased copolymers: Reactivity ratios, physicochemical characterization and cytotoxicity, Eur. Polym. J., 2022, 178, 111478, DOI: 10.1016/j.eurpolymj.2022.111478.
- 26 I. Chaduc, M. Girod, R. Antoine, B. Charleux, F. D'Agosto and M. Lansalot, Batch Emulsion Polymerization Mediated by Poly(methacrylic acid) MacroRAFT Agents: One-Pot Synthesis of Self-Stabilized Particles, Macromolecules, 2012, 45(15), 5881-5893, DOI: 10.1021/ma300875y.
- 27 O. J. Deane, P. Mandrelier, O. M. Musa, M. Jamali, L. A. Fielding and S. P. Armes, Synthesis and

- Characterization of All-Acrylic Tetrablock Copolymer Nanoparticles: Waterborne Thermoplastic Elastomers via One-Pot RAFT Aqueous Emulsion Polymerization, Chem. 2061-2075, DOI: 10.1021/acs. Mater., 2024, 36(4), chemmater.3c03115.
- 28 Z. Zhang, H. Sun, J. Giannino, Y. Wu and C. Cheng, Biodegradable zwitterionic polymers as PEG alternatives for drug delivery, J. Polym. Sci., 2024, 62, 2231-2250, DOI: 10.1002/pol.20230916.
- 29 A. E. Efraim Alexakis, M. R. Telaretti Leggieri, T. Benselfelt and E. Malmström, Modification of CNF-Networks by the Addition of Small Amounts of Well-Defined Rigid Cationic Nanolatexes, J. Colloid Interface Sci., 2023, 634, 610-620, DOI: 10.1002/macp.202200249.
- 30 A. B. Fall, S. B. Lindström, O. Sundman, L. Ödberg and L. Wågberg, Colloidal Stability of Aqueous Nanofibrillated Cellulose Dispersions, Langmuir, 2011, 27(18), 11332-11338, DOI: 10.1021/la201947x.
- 31 A. J. Benítez and A. Walther, Cellulose nanofibril nanopapers and bioinspired nanocomposites: a review to understand the mechanical property space, J. Mater. Chem. A, 2017, 5(31), 16003-16024, DOI: 10.1039/c7ta02006f.
- 32 A. Kulachenko, T. Denovelle, S. Galland S. B. Lindström, Elastic properties of cellulose nanopaper, Cellulose, 2012, 19(3), 793-807, DOI: 10.1007/s10570-012-9685-5.
- 33 M. Henriksson, L. A. Berglund, P. Isaksson, T. Lindström and T. Nishino, Cellulose Nanopaper Structures of High Toughness, Biomacromolecules, 2008, 9(6), 1579-1585, DOI: 10.1021/bm800038n.
- 34 B. D. Mattos, B. L. Tardy, L. G. Greca, T. Kämäräinen, W. Xiang, O. Cusola, W. L. E. Magalhães and O. J. Rojas, Nanofibrillar networks enable universal assembly of superstructured particle constructs, Sci. Adv., 2020, 6(19), DOI: 10.1126/sciadv.aaz7328.
- 35 R. Leiner, S. Witayakran, S. Verwaayen, L. Siegwardt, C. C. Ribeiro, C. Dietz, M. Koch, A. Kulachenko and Gallei, Tailored Interaction between Cellulose Nanowhiskers and Core-Shell Particles Determines the Optical and Mechanical Properties in Hybrid Films, ACS Appl. Mat. Interfaces, 2024, 16, 64377-64387, DOI: 10.1021/ acsami.4c16816.